Proceedings of ASME Tubbo Expo 2016:Turbomachinery Technical Conference and Exposition
GT2016
June 13-17, 2016, Seoul, Korea

GT2016-57985

DELAYED DETACHED EDDY SIMULATION OF ROTATING STALL FOR A FULL ANNULUS TRANSONIC AXIAL COMPRESSOR STAGE

Jiaye Gan *
Hong-Sik Im †
Ge-Cheng Zha‡
Dept. of Mechanical and Aerospace Engineering
University of Miami
Coral Gables, Florida 33124
E-mail: gzha@miami.edu

ABSTRACT

This paper solves the filtered Navier-Stokes equations to simulate stall inception of NASA compressor transonic Stage 35 with delayed detached eddy simulation(DDES). A low diffusion E-CUSP Riemann solver with a 3rd order MUSCL scheme for the inviscid fluxes and a 2nd order central differencing for the viscous terms are employed. A full annulus of the rotor-stator stage is simulated with an interpolation sliding boundary condition (BC) to resolve the rotor-stator interaction. The tip clearance is fully gridded to accurately resolve tip vortices and their effect on stall inception. The DDES results show that the stall inception of Stage 35 is initialized by a weak harmonic disturbance with the length scales of the full annulus and grows rapidly with two emerging spike like disturbance. The two spike disturbances propagate in counter rotational direction with about 42% of rotor speed. The spike stall cells cover about 6 blades. They lead to two stall cells grown circumferentially and inwardly.

Nomenclature

BC	Boundary Condition
CUSP	Convective Upwind and Splitting Pressure
DES	Detached Eddy Simulation
DDES	Delayed Detached Eddy Simulation
LES	Large Eddy Simulation
T	Time used in one rotor revolution
URANS	Unsteady Reynolds-Averaged Navier-Stokes
WENO	Weighted Essentially Non-Oscillatory

Introduction

High fidelity prediction of turbulent flows is very important for accurate simulation of rotating stall characteristics with three-dimensional vortical flows, nonlinear shock wave-boundary layer interaction, and different time scale of disturbance cells in high speed axial compressor. These features play important roles in the formation of stall cells characterized by propagating speed and number of cells in an annulus. Accurate prediction of the number of cells and their speeds is important since their product will give the frequency of stall cells passing each blade. If such a frequency is near a natural frequency of the blade, resonance may occur and result in mechanical failures of the blade. Accurate simulation of unsteady stall inception flows is challenging for Reynolds-averaged Navier-Strokes (RANS) methods since RANS models intend to model the large scale eddies using a universal model. Large scale turbulence structures are affected by the flow geometry and boundary conditions and a universal model does not exit. Large Eddy Sim-

*ASME Member, Ph.D. Student
†ASME Member, Ph.D., Currently an engineer at Honeywell
‡Professor, ASME Fellow

ulation(LES) is considered as more accurate methodology than RANS since LES directly simulates the large eddies and models the small eddy structures that are more isotropic. However, LES requires excessive CPU time for realistic high Reynolds number engineering problems, in particular resolving wall boundary layers demands very fine mesh near the walls.

To overcome the intensive CPU requirement for LES, Spalart developed the detached eddy simulation (DES) strategy [1], which is a hybrid RANS and LES method. Near the solid surface within the wall boundary layer, the unsteady RANS model is realized. Away from the wall surface, the model automatically converts to LES. By using the RANS model near walls, the mesh size as well as the CPU time can be substantially reduced. It is shown [1–3] that the use of hybrid RANS/LES approaches is very effective for stalled flow predictions. Delayed detached-eddy simulation (DDES) by Spalart [4] is an improved version of the original DES97 model. In the framework of DDES, a blending function similar to the one used by Menter and Kuntz [5] for the SST model is introduced to limit the DES length scale to ensure the transition of RANS to LES be independent of grid spacing. The DDES model demonstrates excellent agreement with experiment and a significant improvement over the DES97 for the various tested cases presented [4]. Im et al [6] conducted full annulus simulation of stall inception for an axial transonic single rotor by using URANS and DES. Their results show that DES predicts the stall inception more realistically than the URANS.

The stall inception of NASA Stage 35 is investigated by several research groups. Bright et al. [7] performed rig test to investigate the stall inception of Stage 35 by considering 5 different conditions. Their results show that the stall inception is a modal type at clean-inlet condition. Mina et al. [8] carried out numerical simulation of rotating stall inception for NASA Stage 35 using a single blade passage. It is observed that at near stall, the tip vortex grows larger in size and its trajectory becomes perpendicular to the main axial flow. A low-momentum area near rotor tip leading edge causes the flow spillage and leads to stall inception. Davis and Yao [9] also used NASA stage 35 single blade passage to investigate stall inception. Their finding agrees with Hoying et al. [10] who show that the circulation of tip clearance vortex plays an important role in stall inception development. Vo [11] conducted rotating stall simulation for a low speed rotor with relative tip Mach number of 0.2 and the transonic NASA stage 35 rotor using 6 blade passages. Their results indicate that leading edge tip clearance flow has spillage below blade tip and back flow at the trailing-edge at the onset of spike. Chen et al. [12, 13] conducted a full annulus simulation of NASA Stage 35 at the full speed using an URANS model. In their simulation, a simplified "roof top" type tip clearance mesh is used to model the tip clearance flow. Their results show that a disturbance first travels at the rotor speed, and then changes to a spike disturbance propagating at 84% rotor speed consisting with multiple stall cells. The disturbance eventually forms a single rotating stall cell of 43% rotor speed [12]. Gan et al. [14] conducted full annulus simulation of the stall inception of Stage 35 by using URANS method. A spike type of stall cell which covers about 6 blade passages and propagates with about 90% of rotor speed was captured.

The objectives of this paper are to use DDES of turbulence to simulate the stall inception of NASA Stage 35, and to reveal the rotating stall mechanism for the high speed axial compressor involving strong shocks with the low diffusion shock capturing scheme.

Numerical Methods

The unsteady spatially filtered Navier-Stokes equations are solved in a rotating frame [15] with the delayed detached eddy simulation (DDES) of turbulence suggested by the Spalart [4]. An accurate shock capturing scheme is necessary to simulate high-speed axial compressors since most rotor blades experience shock/boundary layer interaction. In this study the Low Diffusion E-CUSP (LDE) Scheme [16] as an accurate shock capturing approximate Riemann solver is used with a 3rd order WENO reconstruction for inviscid flux and a 2nd order central differencing for viscous terms [17]. An implicit 2nd order dual time stepping method [18] is solved using an unfactored Gauss-Seidel line iteration to achieve high convergence rate. The high-scalability parallel computing is applied to save wall clock time [19].

Delayed Detached Eddy Simulation

In DES, the Spalart-Allmaras(S-A) model is modified to keep its form within wall boundary layer and switches to a subgrid scale formulation in regions for LES calculations. The coefficients c_{t1} and c_{t3} in the S-A model are set to zero and the distance to the nearest wall, d, is replaced by $\tilde{d}$ as

$$\tilde{d} = min(d, C_{DES}\Delta) \tag{1}$$

where Δ is the largest spacing of the grid cell in all the directions. Within the boundary layer close to the wall, $\tilde{d} = d$, hence the turbulence is simulated by RANS mode of Spalart-Allmaras [20]. Away from the boundary layer, $\tilde{d} = C_{DES}\Delta$ is most of the cases. When the production and destruction terms of the model are balanced, the length scale $\tilde{d}$ will have a Smagorinsky-like eddy viscosity and the turbulence is simulated by the LES model. The coefficient $C_{DES} = 0.65$ is used as set in the homogeneous turbulence [2]. The Pr_t may take the value of 0.9 within the boundary layer for RANS mode and 0.5 for LES mode away from the wall surface.

To overcome the modeled stress depletion problem and make the DES limiter independent of grid spacing, the DDES

model suggested by Spalart et al. [4] switches the subgrid scale formulation in S-A model by redefining the distance to the nearest wall $\tilde{d}$ as

$$\tilde{d} = d - f_d max(0, d - C_{DES}\Delta) \tag{2}$$

where

$$f_d = 1 - tanh([8r_d]^3) \tag{3}$$

$$r_d = \frac{\nu_t + \nu}{\sqrt{U_{i,j}}k^2 d^2 R_e} \tag{4}$$

$$U_{i,j} = \frac{\partial u_i}{\partial x_j}\frac{\partial u_j}{\partial x_i} \tag{5}$$

where Δ is the largest spacing of the grid cell in all the directions, $U_{i,j}$ represents the velocity gradient tensor, and k denotes the Karmann constant. Within the boundary layer close to walls, $\tilde{d} = d$, and away from the boundary layer, $\tilde{d} = C_{DES}\Delta$ is most of the case. This mechanism enables DDES to behave as a RANS model in the near-wall region, and LES away from walls. This modification in $\tilde{d}$ reduces the grey transition area between RANS and LES.

The validation of current DDES methodology for the stalled flow over NACA0012 airfoil at 45° angle of attack was accomplished by Im et al. [3]. The DDES predicts the drag accurately compared to the experiment, whereas the URANS model over predicts the drag by about 33%.

Boundary condition

For unsteady rotor-stator interaction simulation, the rotor mesh will rotate with the rotor blades and the stator mesh will be stationary. Solving the Navier-Stokes equations requires transferring the fluxes between these two meshes. In [21], a conservative sliding BC is developed by making the meshes on both side of the sliding boundary one-to-one connected. Even though the conservative BC is mathematically more rigorous, it is not always convenient to make a multi-block mesh one-to-one connected. For engineering applications, independent mesh for rotor and stator is desirable for efficient setup of a simulation. This paper thus adopts an interpolation sliding BC [14] with high accuracy to remove the requirement that the rotor and stator mesh needs to be one-to-one connected.

At the inlet, the radial distributions of total pressure, total temperature, swirl angle and pitch angle are specified and the velocity is extrapolated from the computational domain in order to determine the rest of the variables. In this paper, no inlet perturbations are used to trigger the stall inception in order to keep the same operation condition as that in [7, 12]. On the blade surface a non-slip boundary condition is applied, while an efficient wall function BC [15] is used on the hub/casing surface where y^+ is greater than 11 to avoid an excessive fine mesh in the end-wall boundary layer. At the stator outlet, a static pressure profile is specified in the spanwise direction. The velocity components are extrapolated from the computational domain and an isentropic relation is used to determine density. The hub/casing wall static pressure for the inviscid momentum equation is determined by solving the radial equilibrium equation, whereas the static pressure gradient across the wall boundary is set to zero for the blade wall surface. An adiabatic condition is used to impose zero heat flux through the wall.

Computational Grid

The transonic axial compressor, NASA stage 35 that consists of 36 rotor blades and 46 stator blades [22], is simulated to investigate the stall inception mechanism. The total pressure ratio of NASA stage 35 at design speed of 17189 rpm is 1.82. The full annulus of Stage 35 geometry and mesh are shown in Fig.1. The mesh size and distribution is outlined here for completeness. An O-mesh topology around blades and H-mesh for stage inlet/outlet duct region are used. For the rotor and stator, $121 \times 69 \times 45$ is the grid dimension in the direction around the blade, blade to blade, and span respectively. The rotor tip clearance is modeled using a fully gridded O-mesh with mesh size of $121 \times 15 \times 11$ as shown in bottom plot in Fig. 1. Within the tip clearance, 11 grid points are placed radially.

The tip gap is shown to have a significant effect on overall performance of axial compressors [23]. The fully gridded tip mesh generation technique adopted in this study is shown to better predict the tip clearance flow than the pinched tip or simplified tip model [24]. In the model of the fully gridded tip, about 4 to 10 points in the tip clearance are generally considered as adequate to predict the primary effects of the leakage flow in axial compressor [13, 15, 23–25]. A non-gridded tip model is used by Chen et al [12]to investigate the pre-stall behavior of NASA Stage 35. Their results indicated that the inception type of the rotating stall can be captured without fully gridded tip model. However, it is not possible to determine the precise impact of the tip clearance modeling on stall inception due to the lack of detailed flow measurements in the tip clearance of NASA Stage 35 during rotating stall.

The effect of grid size on solution accuracy for Rotor 37 using H-O-H grids with O-grid tip clearance region by McNulty

[24] shows remarkably similar predictions using three grid size approximately with 200,000, 350,000 and 400,000 points. Similar results are obtained for the mesh refinement study using the rotor-alone single passage in their study. Their mesh size is similar or coarser than what we used. Im et al. [15] uses a NASA Rotor 67 full annulus mesh with about 7 million grid points to capture the stall cell rotating at about 48% of rotational speed. The mesh size and distribution of a single blade used by Im et al. [15] is also similar to what are used in this paper. The steady state mesh refinement study was conducted in [14]. The mesh is mainly refined around the blade, which has the dimension of $201 \times 77 \times 51$. The results indicates that the solution is converged based on the chosen mesh size. The excellent agreement between the predicted radial profiles of NASA Stage 35 compared with the experiment also evidences that the mesh is fine enough to resolve the wakes. The low diffusion E-CUSP scheme employed in the paper also contributes to minimize the numerical diffusion and hence mesh size

Considering a disturbance with its wavelength on the order of the circumference, it is desirable to locate the inlet and outlet boundary of the computational domain far away from the rotor blade. In this study the inlet plane are located about 8 axial tip chord length upstream of the rotor and about 6 axial tip chord length downstream of the stator. Total mesh points of the full annulus are about 16 million with 482 blocks.

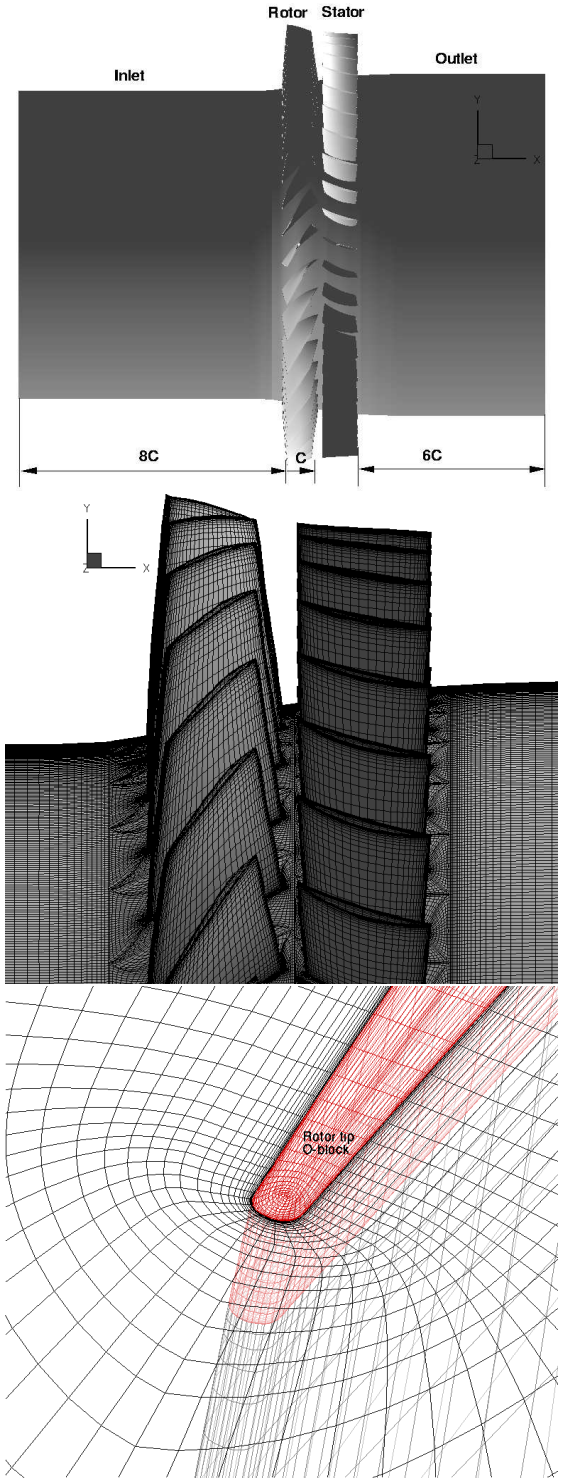

FIGURE 1: Full annulus mesh of NASA stage 35

Results and discussion

The full annulus unsteady simulation begins with near stall(or near peak of the rotor characteristics) solutions obtained by the RANS simulation [26]. This approach is employed by other researchers [10, 11, 27] for the rotating stall simulations in order to reduce computing efforts.

A physical time step of around 0.000009 sec. is used in this study. And one rotor revolution will take 1440 steps. The study by Copenhaver et al. [28] shows a time step of 0.00025 sec. is necessary to capture shock instability in a transonic rotor. Hah et al. [29] used a time step of 0.0000125 sec. for predicting the stall inception of a similar high speed rotor originated by the interaction of the passage shocks and tip leakage vortices. As aforementioned, the rotating speed of the spike type stall cell in a high-speed compressor is roughly half of the rotor rotational frequency [30, 31], the time step size adopted in this study is significantly smaller than those used by all other researchers and is sufficient to resolve the primary flow features during the stall inception.

Fig. 2 shows the L2 norm residual and inlet mass flow rate converging history obtained by the RANS at choke and DDES during rotating stall. Due the strong shock occurred near the rotor leading edge, the RANS calculation began with a 1/3 of designed rotor speed. Once the computation has converged enough (for 10000 steps the calculation converged about 5 orders of magnitude) as shown in the top plot of Fig. 2, the results can be used

to start full speed simulation. The step changes in residual and mass flow rate around 10000 steps are due to the change of RPM. The unsteady simulation achieves 2 orders of magnitude residual reduced in each physical time step. The calculation becomes numerically unstable after 3.2 rotor revolutions. The maximum residual occurred at rotor stator interface, which may be due to the high aspect ratio mesh was used near the casing surface.

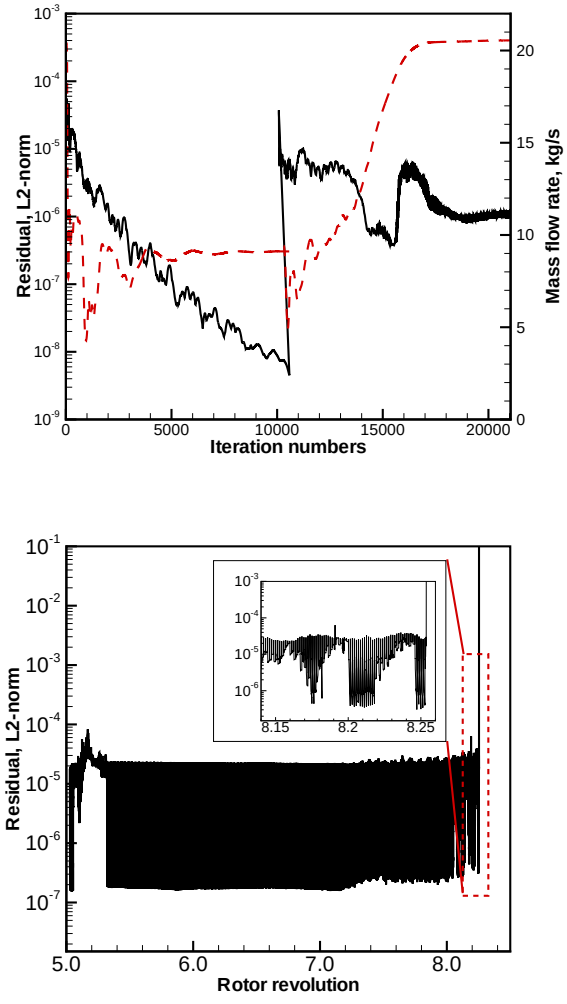

FIGURE 2: Convergence history: RANS(top),DDES(bottom)

Stall Pressure Rise Characteristics

The predicted unsteady stage speed line is illustrated in Fig.3, which starts from the near stall point D. From point A to point D, the simulation is steady state and the results at point D are used as initial flow field of the unsteady calculation. The rotating stall inception simulation begins at point P1 with the back pressure fixed and letting the stall inception developing by itself. The stage total pressure ratio drop is slow from point P1 to point P2. And the total pressure ratio decrease rapidly after point P2, which indicates the onset of rotating stall. Large pressure ratio oscillation is observed between point P4 and P5. The unsteady calculation diverged at point P6 due to numerical instability. Fig.4 shows the variations of mass flow rate calculated near rotor leading edge during rotating stall. The mass flow drops slowly at the first 2T (T is the time of one rotor revolution) from point P1 to P2 and starts oscillating after that. The major stalling phenomenon at P5 is that rotating stall quickly grows toward inner span with the occurrence of the two stall cells, which will be further discussed in the following sections.

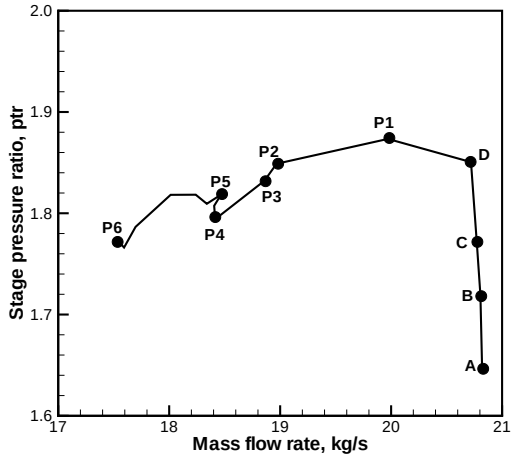

FIGURE 3: Predicted unsteady speed line with full annulus simulation

Rotating Stall Onset and Propagation

Rotating stall is usually initiated from rotor tip. This is also the case for the NASA Stage 35. To capture the rotating stall inception, the numerical probes are located about 50% tip chord length upstream and downstream at the rotor tip span. The term 'stall cell' used in the current study is to describe a continuous structure of disturbances.

Fig.5 shows the variations of instantaneous static pressure and axial velocity at the rotor tip upstream. Small amplitude of pressure fluctuations that is about 0.8% of the average pressure are observed near 7.0T, which cover about full annulus of the compressor and appear to be modal disturbance. Generally,

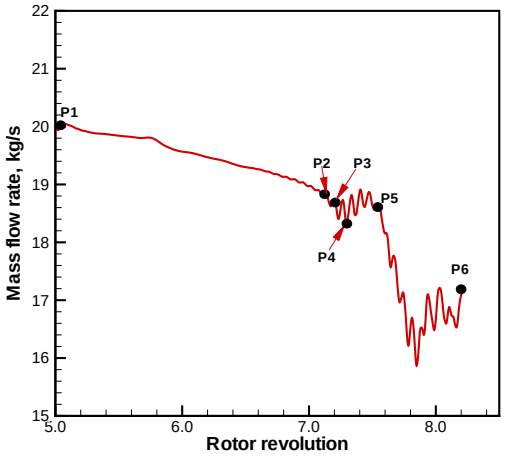

FIGURE 4: Mass variation during stall

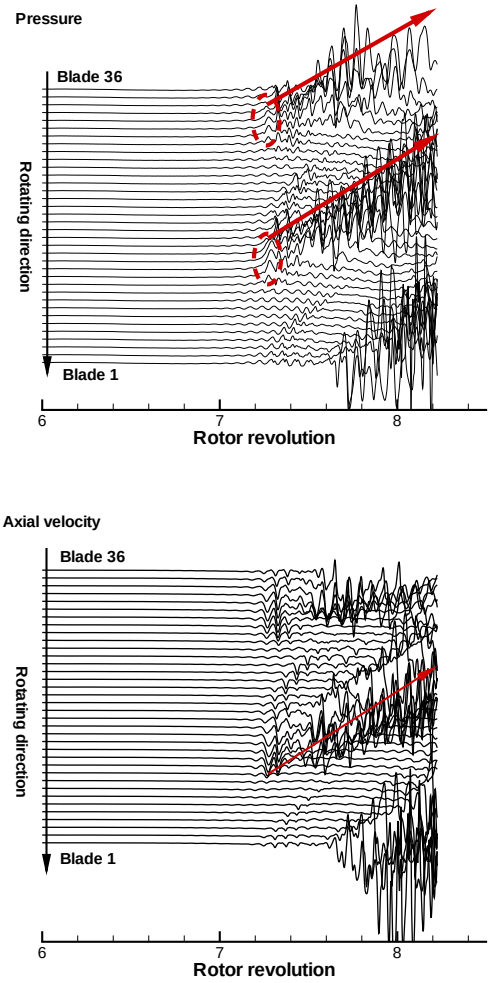

FIGURE 5: Time traces of pressure and axial velocity near half tip chord length upstream of the rotor leading edge at the tip span

the modal disturbance has a length scale of one rotor circumferential and propagates with about 20% to 50% of rotor speed. The modal disturbance obsered in this paper does not propagate, which is different from the classical modal wave. At about 7.3T, two spike disturbances with amplitude about 10.0% of the local pressure appear. The propagation arrows shown in plots are obtained by roughly connecting the peak of pressure in adjacent passage. The propagating speed of stall cell can be determined by the slope of the line. The two disturbances rotate at about 42% rotor speed. Large mass flow fluctuations are seen during the stall inception as shown in Fig. 4.

After about 1T counted from the emergence of the two spike like inception stall cells(P2), the numerical simulation becomes unstable before the fully developed stall cells are captured. However, it does not affect the investigation of stall inception mechanism that is far before the fully developed stall cells are formed. The trigger of stall inception is flow instability instead of numerical instability, since the residual is less than 10^{-5} and 2 orders of magnitude residual reduction is achieved as shown in Fig. 2. The calculation diverged quickly in a few pseudo time iteration within one physical time step.

The time traces of pressure and axial velocity located at rotor stator interface are presented in Fig. 6. Two main rotating stall cells are also observed in the plots, which indicate the axial range of the stall cell is at least from the leading edge to the interface. The propagating speed of the two stall cells are almost the the same as that observed in the rotor upstream plots, but the propagating direction of the stall cells at downstream of rotor is opposite to that at rotor upstream in relative frame. Furthermore, the rotating stall at the downstream of the rotor starts about 0.1T earlier than that at the upstream, which may be due to the rotor stator interaction.

In the stall simulation of Stage 35 by Chen et al. [12] modal disturbance is observed at the first 2 rotor revolutions and then it transforms into spike disturbance. The modal disturbance in their study is not a classical one too, because the propagating speed is 100% of rotor speed. The forming process of the spike disturbance in this paper has similar pattern, but occurs more rapidly. From the modal wave to spike, the present simulation has only 0.3 rev. However, the spike disturbances captured in this paper are more compact, covering about 6 blade passages. The number and size of stall cells can not be observed in the similar plot of time trace of pressure in the results of Bright et al. [7] and Chen et al. [12], since there are only 8 numerical probes located near

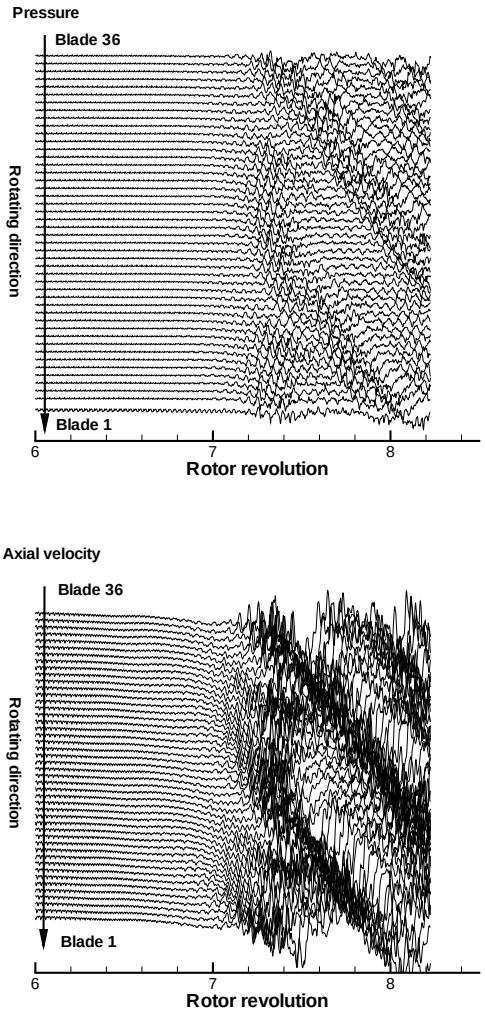

FIGURE 6: Time traces of pressure and axial velocity near half tip chord length downstream of the rotor trailing edge at the tip span

the rotor leading edge. Casing wall static pressure measurements of Stage 35 by Bright et al. [7] shows the spike(pip) inception is a disturbance standing on the modal wave. This phenomenon is not clearly seen in the numerical results of Chen et al. [12], Gan et al. [14] and this paper. The variation of axial velocity follows the same behavior as that of pressure, as shown in Fig. 5 but the propagating speed of the stall cell is more clear. We can roughly calculate the propagating speed of the stall cell from the velocity plot.

The circumferential static pressure time history can be also used to investigate the stall inception characteristics. Fig.7 shows the circumferential distributions of the normalized static pressure and velocity located at 50% tip chord upstream of rotor at different time. At t=7.0T(P1), the flow around the full annulus is periodic and no disturbances are observed. The variation of static pressure through full annuls appears to have sharp shape, which indicates that there exit strong shock waves near the leading edge of the rotor. At t=7.25 T(between point P3 and P4), the flow periodicity is lost at some parts of the annulus, and the annulus region containing large disturbance are from $90^\circ \sim 150^\circ$ for the first stall cell, and $280^\circ \sim 340^\circ$ for the second stall cell, which indicate that the sizes of the stall cell at this moment cover about 5 to 6 passages. The local non-uniform pressure indicates the onset of the spike type rotating stall. After about 1T from the stall inception point P2, the rotating stall reaches point P6. Fig. 7 shows that the sharp edge shapes of pressure distribution disappear after t=7.25T in the stall cell region due to the shock waves moving to upstream.

In the Stage 35 rotating stall simulation by Gan et al. [14], the predicted propagating speed of stall cell by using URANS method is about 90% of rotor speed, which is about two times of the DDES. The mass flux in circumferential direction at 7.33T, as shown in Fig. 8 may be used to understand the cause of the speed difference in the methods of URANS and DDES. It is seen that the amplitude of circumferential mass flux oscillation predicted by the URANS is about the same as the DDES at the mid span where there no stall flow. However, the amplitude of the mass flux oscillation at stall region predicted by the URANS at tip span is about two times greater than that of the DDES. The large gradient of tangential mass flux between the stalled region and unstalled region may cause the stall cell propagating with such high speed in the URANS. It appears that the propagating speed of rotating stall is determined by the circumferential mass flux oscillation in relative frame.

Fig. 9 and Fig. 10 illustrate entropy contours in axial cross section near the rotor leading edge and trailing edge. Entropy stands for the degree of energy loss and high entropy reflects the stalled portion of the annulus. At 7.33T(near stall onset), two continuous high entropy regions near casing surface can be seen in Fig. 9. The primary stall cell is identified by about 5 stalled passages. It is shown that the stall cell starts from the rotor tip area, and grows along the circumference as well as inward. The high entropy region near the rotor trailing edge cover the full annulus at 7.33T as shown in Fig. 10. The tip leakage vortices, separation vortices on suction surface, and trailing edge vortices may contribute to the loss of energy in the annulus at stall condition. The interaction of those vortices with stator blades may cause the flow to stall earlier at the rotor downstream.

Fig. 11 shows the entropy line contours during rotating stall. The axial length scale of the stall cell at 7.33T is about one tip chord length. As the stall cells develop, the flow blockages extend both upstream and downstream of the rotor.

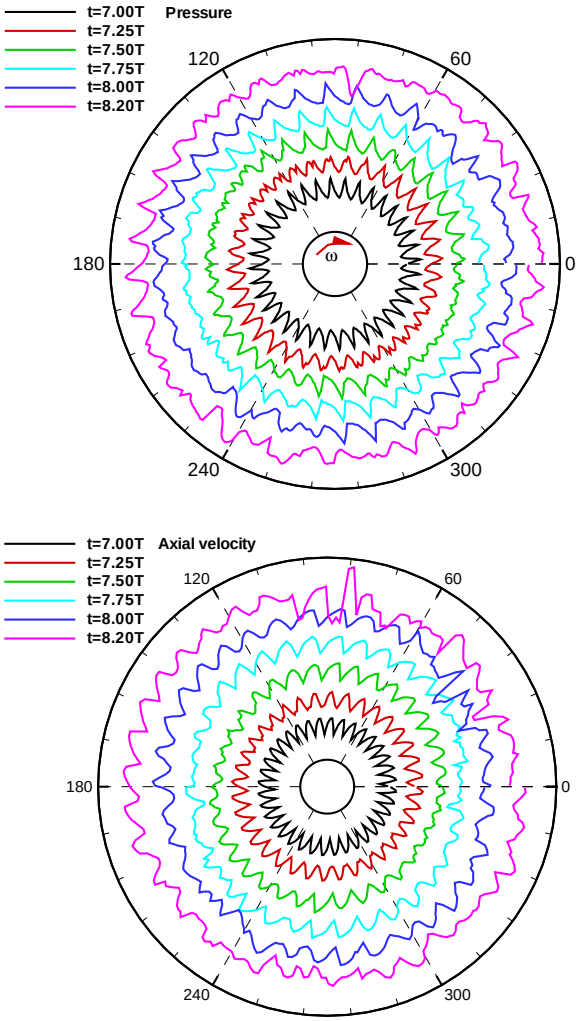

FIGURE 7: Circumferential variations of pressure(Top) and axial velocity(Bottom) at tip span

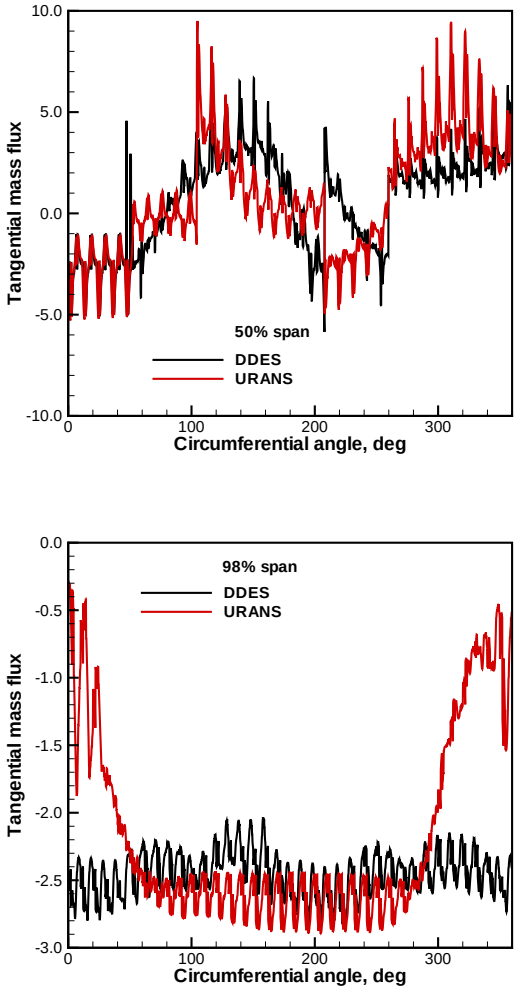

FIGURE 8: Relative circumferential flux at the mid span(Top) and tip span(Bottom) near rotor leading edge

Flow mechanism of rotating stall

Fig. 12 shows the relative velocity vector and Mach number contour indicating the sonic boundary at the tip span. The plots are used to track the stall cell in the annulus. At 7.11T, before the onset of rotating stall, the sonic lines is attached and oblique to the rotor leading edge. And there are no back flow observed from the rotor trailing edge. At 7.33T, the stall onset point, a large vortex is formed in each blade passage near the rotor tailing edge. The through flow is largely blocked by the vortex. The sonic boundary becomes detached off the leading edge, which is caused by the flow blockage. At 8.0T, the stall cells grows larger and the sonic line is pushed further upstream by the flow blockage. The vortex moves upstream and interacts with tip leakage flow, which forms a large vortex located in the middle of the blade passage near the rotor leading edge.

The instantaneous contours of static pressure at the tip span are shown in Fig.13. It can be seen that the spike stall inception region has higher blockage that generates high pressure wave propagating upstream, which destroys the circumferential periodicity. As the rotor rotating, the stall cell propagates in the opposite direction of rotor revolution in relative frame as shown in Fig. 9 and grows rapidly. The flow blockage becomes larger with time at 8.0T, the non-periodic flow near the tip span covers most of the rotor passages. Furthermore, it is evident that the rotating stall is convected downstream of rotor and interacts with stator, which creates a significant blockage in the stator blades.

The vortex structures during rotating stall near the rotor tip span are shown in Fig. 14. At 7.11T, before stall inception, the

oblique tip leakage vortices are the main turbulent flow structure in the rotor blade passage. And no trailing back flows are seen at this instant. At 7.33T, the stall inception point, it can be seen that a large vortex is developed near the mid-chord on the suction surface. The interaction of leading edge separation vortex with tip leakage flow is the cause of the vortex. The sonic boundary is moved upstream by this vortex as shown in Fig. 12. And at the same instant, there is a vortex with its axis in radial direction near the trailing edge on suction surface, which can be observed in the middle plot of Fig. 12. The interaction of tip leakage flow with the trailing vortex create an infant pitchwise vortex in the blade passage. At 8.22T, there are three main vortices formed in the blade passage that are covered by the stall cell as shown in Fig. 12. The vortex V1 is mainly formed by the interaction of the tip leakage flow with the leading edge separation flow. The vortex V2 is formed by part of the tip leakage flow and trailing edge back flow. The vortex V3 is mainly from the trailing edge back flow. The flow at the stalled region near tip section are mainly blocked by these three vortices.

Conclusions

The full annulus DDES is conducted for the first time to investigate rotating stall inception mechanism of the transonic Stage 35 with sliding interpolation BC. The details of the flow breakdown that leads to fully developed rotating stall is well captured by the present numerical simulation. The simulation shows that the rotor stall onset begins with modal disturbance followed rapidly by two spike disturbance. The size of the onset stall cell cover about 5 to 6 rotor blade passages. The propagation speed of stall cell is about 42% of rotor rotating speed. This DDES of stall inception captures two stall cells whereas the previous URANS simulation only has one stall cell propagating at about 90% rotation speed. The different propagating speed of stall cells between the URANS and the DDES may be due to the different circumferential mass flux in relative frame.

The main mechanism captured by the DDES is the trailing edge back flow as the blockage near the tip section that leads to the total pressure drop. The blockage pushes the convecting tip flows upstream, and which leads to the detached shocks from the rotor leading edge. The sonic plane begins to parallel to the rotor leading edge plane during stall inception. As the sonic plane moves upstream of the rotor LE tip by the flow blockage, the stall cell grows and propagates at the speed of 42% in the counter to the roror rotation in relative frame.

Acknowledgment

The computing resource supports from the Center for Computational Sciences at University of Miami are greatly appreciated.

REFERENCES

[1] P.R. Spalart, W.H. Jou, M. Strelets, and S.R. Allmaras, "Comments on the Feasibility of LES for Wings, and on a Hybrid RANS/LES Approach." Advances in DNS/LES, 1st AFOSR Int. Conf. on DNS/LES, Greyden Press, Columbus, H., Aug. 4-8, 1997.

[2] M. Shur, P.R. Spalart, M. Strelets, and A. Travin, "Detached Eddy Simulation of an Airfoil at High Angle of Attack", 4th Int. Symp. Eng. Turb. Modeling and Measurements, Corsica." May 24-26, 1999.

[3] Im, H.S. and Zha, G.C., "Delayed Detached Eddy Simulation of Airfoil Stall Flows Using High Order Schemes," 2014.

[4] P.R. Spalart, S. Deck, M. Shur, and K.D. Squires, "A New Version of Detached Eddy Simulation, Resistant to Ambiguous Grid Densities," *Theoritical and Computational Fluid Dynamics*, vol. 20, pp. 181–195, 2006.

[5] F.R. Menter, and M. Kuntz, "Adaptation of Eddy-Viscosity Turbulence Models to Unsteady Separated Flow Behind Vehilces, *The Aerodynamics of Heavy Vehicles: Trucks, Buses and Trains, Edited by McCallen, R. Browand, F. and Ross, J. ," Springer, Berlin Heidelberg New York, 2004*, 2-6 Dec. 2002.

[6] Im, H.S., Chen, X.Y., Zha, G.C., "Detached-Eddy Simulation of Rotating Stall Inception for a Full-Annulus Transonic Rotor," *Journal of Propulsion and Power*, vol. 28, pp. 782–798, 2012.

[7] Bright, M.M.; Qammar, H.K.; and Wang, L.Z., "Investigation of Pre-Stall Mode and Pip Inception in High-Speed Compressors Through Through the Use of Correlation Integral," *Journal of Turbomachinery*, vol. 121, pp. 743–750, 1999.

[8] M. Zake, L. Sankar, and S. Menon, "Hybrid Reynolds-Averaged Navier-Stokes/Kinetic-Eddy Simulation of Stall Inception in Axial Compressors," *Journal of Propulsion and Power*, vol. 26, pp. 1276–1282, doi: 10.2514/1.50195, 2010.

[9] R. Davis, and J. Yao, "Computational Approach for Predicting Stall Inception in Multistage Axial Compressor," *Journal of Propulsion and Power*, vol. 23, pp. 257–265, doi: 10.2514/1.50195, 2007, doi: 10.2514/1.18442.

[10] D.A. Hoying, C.S. Tan, H.D. Vo, and E.M. Greitzer, "Role of Blade Passage Flow Structures in Axial Compressor Rotating Stall Inception," *AMSE J. of Turbomach.*, vol. 121, pp. 735–742, doi:10.1115/1.2836727, 1999.

[11] H.D. Vo, C.S. Tan, and E.M. Greitzer, "Criteria for Spike Initiated Rotating Stall," *AMSE J. of Turbomach.*, vol. 130, pp. 1–8, doi:10.1115/1.2750674, 2008.

[12] J. Chen, B. Johnson, M. Hathaway, and R. Webster, "Flow Characteristics of Tip Injection on Compressor Rotating Spike via Time-Accurate Simulation," *Journal of Propulsion and Power*, vol. 25, pp. 678–687, doi:

10.2514/1.41428, 2009.

[13] J. Chen, M. Hathaway, and G. Herrick, "Prestall Behavior of a Transonic Axial Compressor Stage via Time-Accurate Numerical Simulation," *AMSE J. of Turbomach.*, vol. 130, pp. 1–12, doi:10.1115/1.2812968, 2008.

[14] Gan, J.Y., Im, H.S., Zha, G.C., "Simulation of Stall Inception of a High Speed Axial Compressor with Rotor-Stator Interaction." AIAA Paper 2015-3932, 51st AIAA/SAE/ASEE Joint Propulsion Conference, Orlando, FL.

[15] H.S. Im, X.Y. Chen, and G.C. Zha, "Detached Eddy Simulation of Stall Inception for a Full Annulus Transonic Rotor," *Journal of Propulsion and Power*, vol. 28 (No. 4), pp. 782–798, doi: 10.2514/1.58970, 2012.

[16] G.C. Zha, Y.Q. Shen, and B.Y. Wang, "An Improved Low Diffusion E-CUSP Upwind Scheme ," *Journal of Computer and Fluids*, vol. 48, pp. 214–220, 2011, doi:10.1016/j.compfluid.2011.03.012.

[17] Y.Q. Shen, G.C. Zha, and B.Y. Wang, "Improvement of Stability and Accuracy of Implicit WENO Scheme," *AIAA Journal*, vol. 47, pp. 331–334, DOI:10.2514/1.37697, 2009.

[18] Y.Q. Shen, B.Y. Wang, and G.C. Zha, "Implicit WENO Scheme and High Order Viscous Formulas for Compressible Flows ." AIAA Paper 2007-4431, 2007.

[19] B. Wang, Z. Hu, and G. Zha, "A General Sub-Domain Boundary Mapping Procedure For Structured Grid CFD Parallel Computation," *AIAA Journal of Aerospace Computing, Information, and Communication*, vol. 5, pp. 425–447, 2008.

[20] P.R. Spalart, and S.R. Allmaras, "A One-equation Turbulence Model for Aerodynamic Flows." AIAA-92-0439, 1992.

[21] H.S. Im, X.Y. Chen, and G.C. Zha, "Simulation of 3D Multistage Axial Compressor Using a Fully Conservative Sliding Boundary Condition." ASME IMECE2011-62049, International Mechanical Engineering Congress & Exposition, Denver, November 2011, 2011.

[22] L. Reid, and R.D. Moore, "Design and Overall Performance of Four Highly-Loaded, High Speed Inlet Stages for an Advanced, High Pressure Ratio Core Compressor." NASA TP.1337, 1978.

[23] J.D. Denton, "Lessons from Rotor 37," *Journal of Thermal Science*, vol. 6, pp. 1–13, doi: 10.1007/s11630–997–0010–9, 1996.

[24] J. Dunham, "CFD Validation for Propulsion System Components." AGARD-AR-355, 1998.

[25] R. V. Chima, "Calculation of Tip Clearance Effects in a Transonic Compressor," *AMSE J. of Turbomach.*, vol. 120, pp. 131–140, 1998.

[26] I.J. Day, and C. Freeman, "The Unstable Behavior of Low and High-Speed Compressors," *AMSE J. of Turbomach.*, vol. 116, pp. 194–201, doi:10.1115/1.2928353, 1994.

[27] H. Khaleghi, M. Boroomand, A.M. Tousi, and J.A. Teixeira, "Stall Inception in a Transonic Axial Fan," *Journal of Power and Energy*, vol. 222, pp. 199–208, doi:10.1243/09576509JPE407, 2008.

[28] W.W Copenhaver, S.L. Puterbaugh, and C. Hah, "Unsteady Flow and Shock Motion in a Transonic Compressor Rotor," *Journal of Propulsion and Power*, vol. 13, pp. 17–23, 1997.

[29] C. Hah, D.C. Rabe, and A.R. Wadia, "Role of Tip-Leakage Vortices and Passage Shock in Stall Inception in a Swept Transonic Compressor Rotor." GT2004-53867, Proceedings of ASME Turbo Expo 2004, 2004.

[30] C. Hah, J. Bergner, and H. Schifer, "Short Length Scale Rotating Stall Inception in a Transonic Axial Compressors : Criteria and Mechanisms." GT2006-90045, ASME Turbo Expo, 2006, doi:10.1115/GT2006-90045.

[31] N. Reuss, and C. Mundt, "Experimental Investigations of Pressure Distortions on the High-Pressure Compressor Operating Behavior," *Journal of Propulsion and Power*, vol. 25, pp. 653–667, doi: 10.2514/1.37412, 2009.

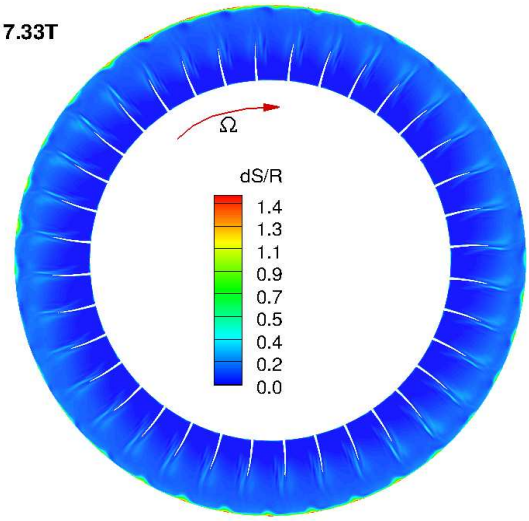

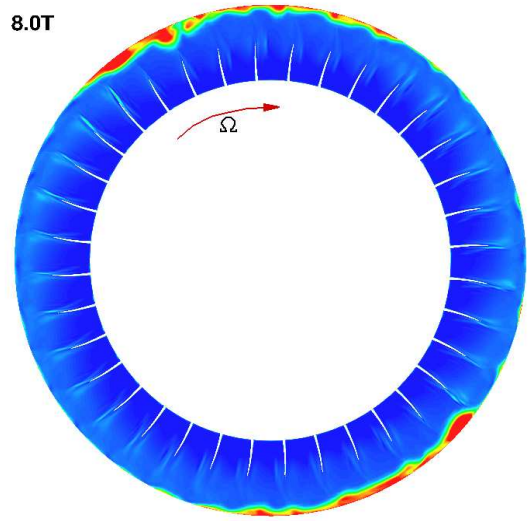

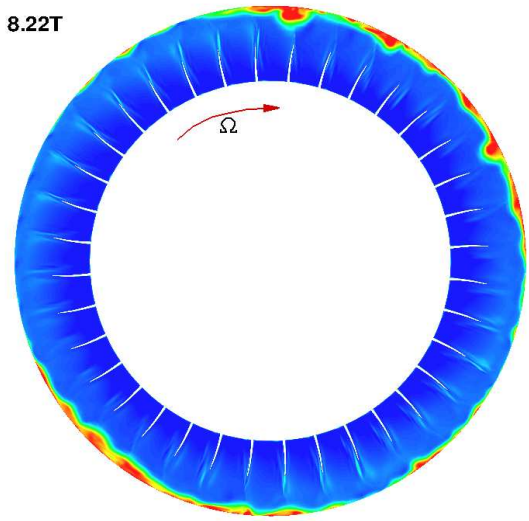

FIGURE 9: Entropy near rotor leading edge

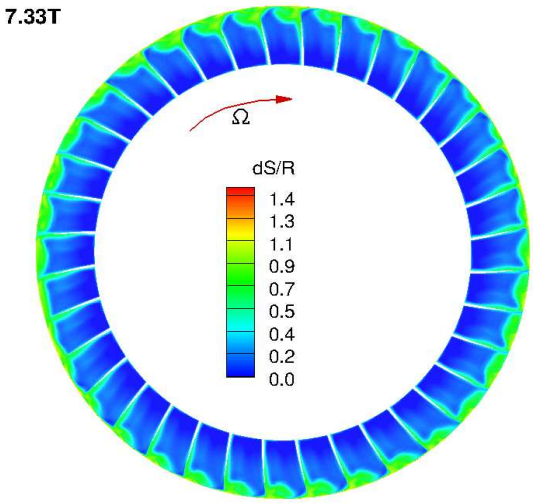

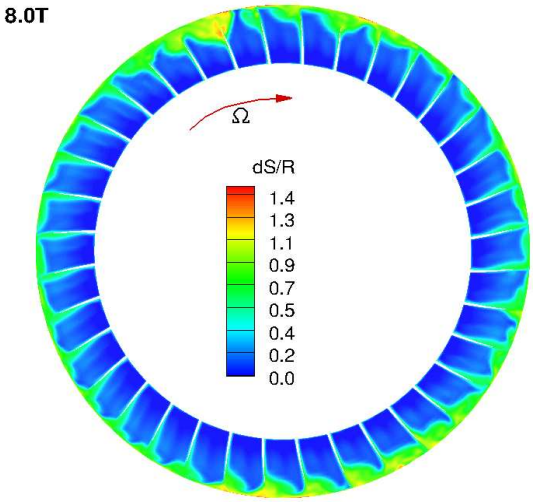

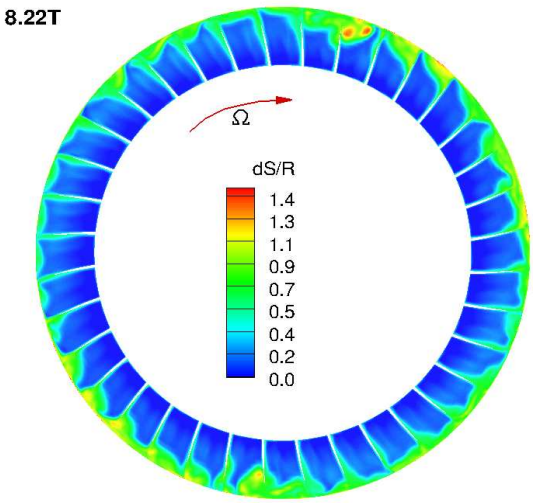

FIGURE 10: Entropy near trailing edge

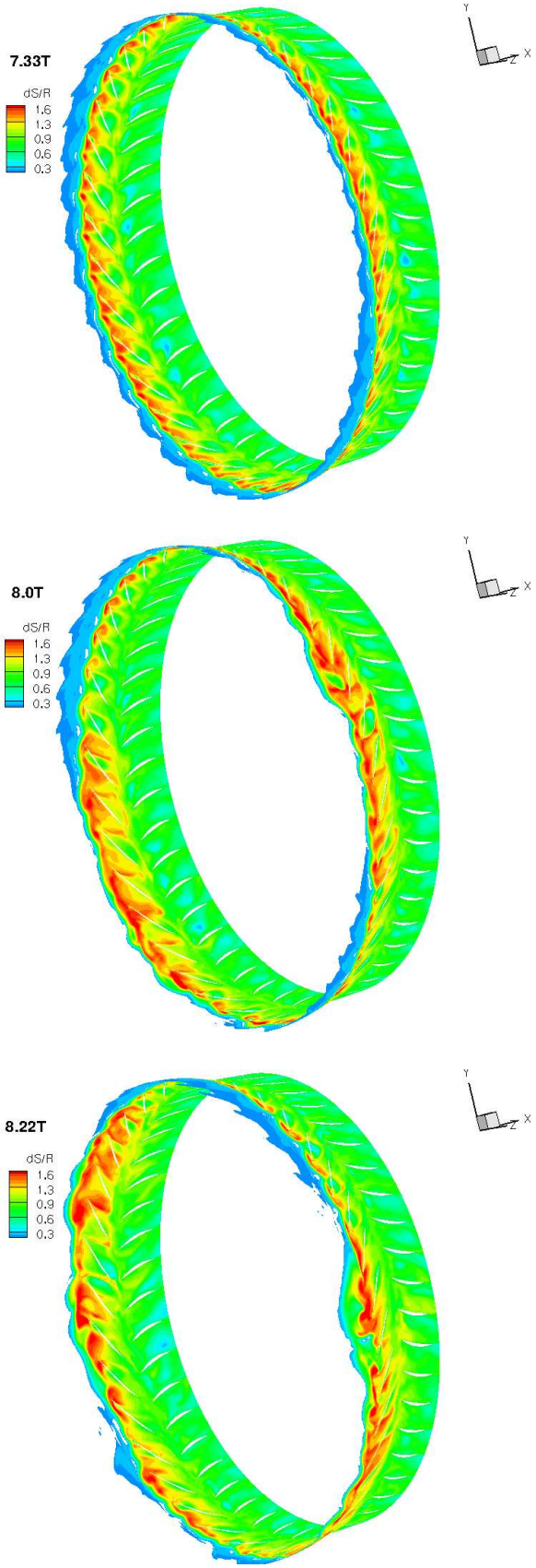

FIGURE 11: Entropy at the mid tip clearance span

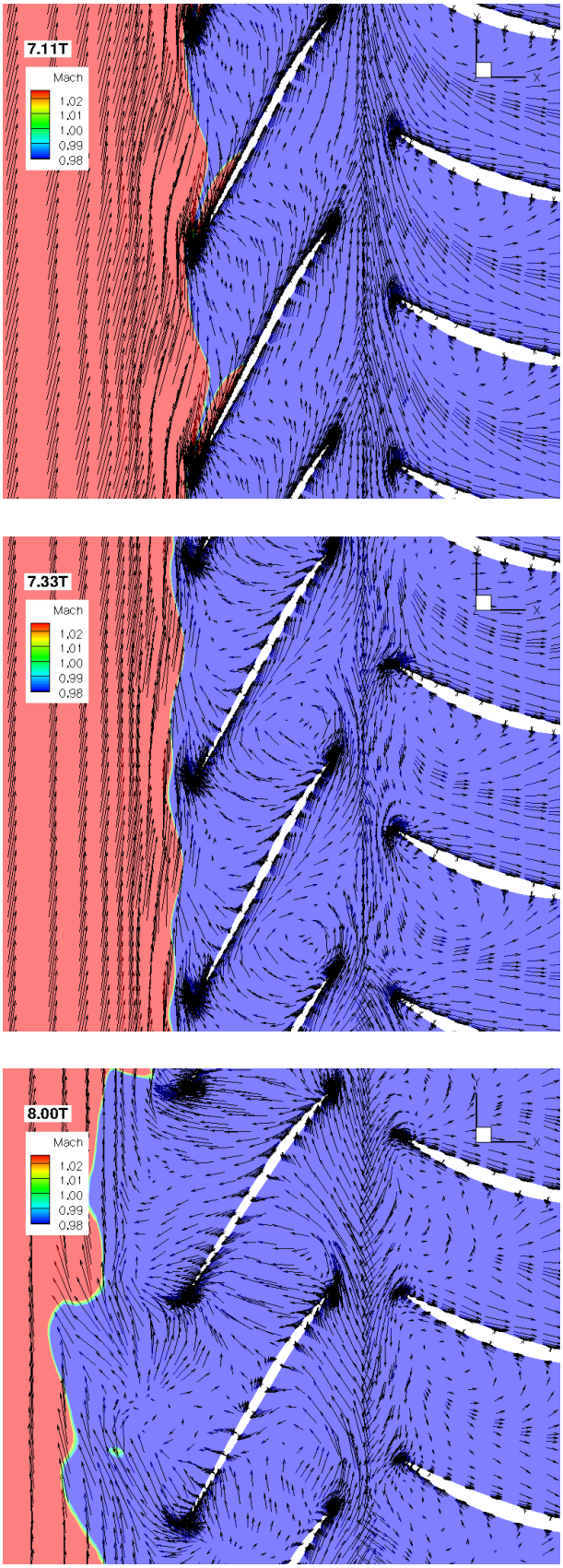

FIGURE 12: Velocity vector of rotor tip span with Mach number contour indicating sonic boundary

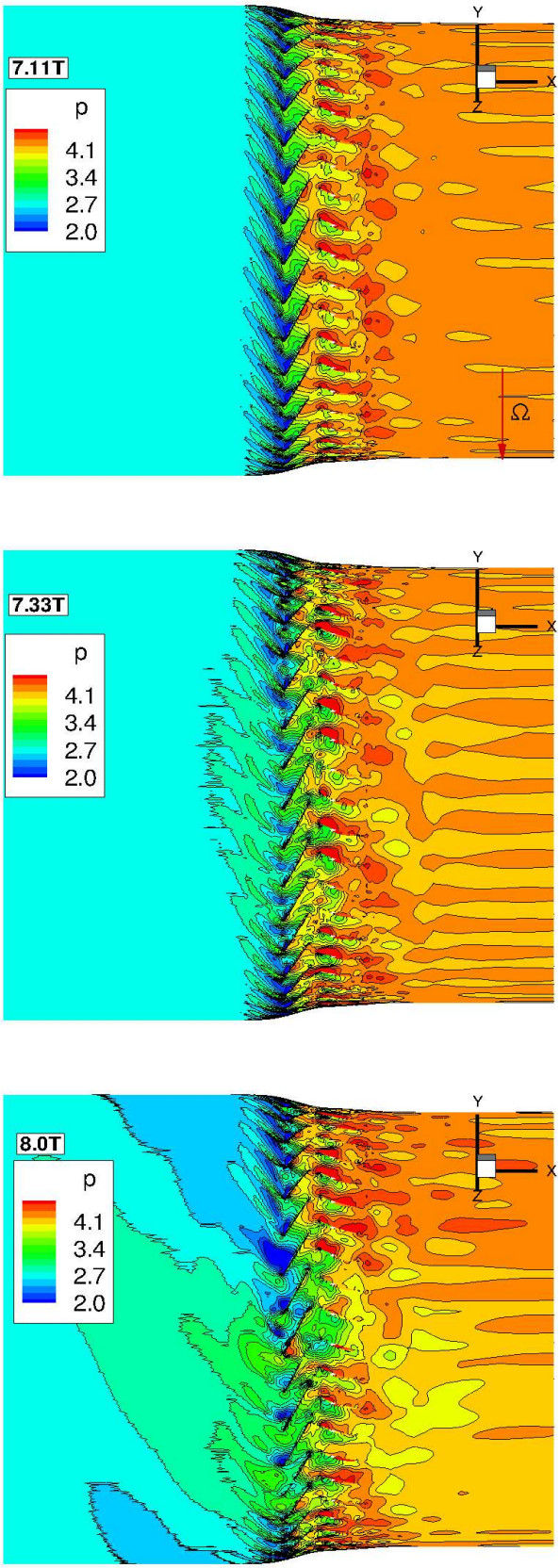

FIGURE 13: Static pressure at the tip span

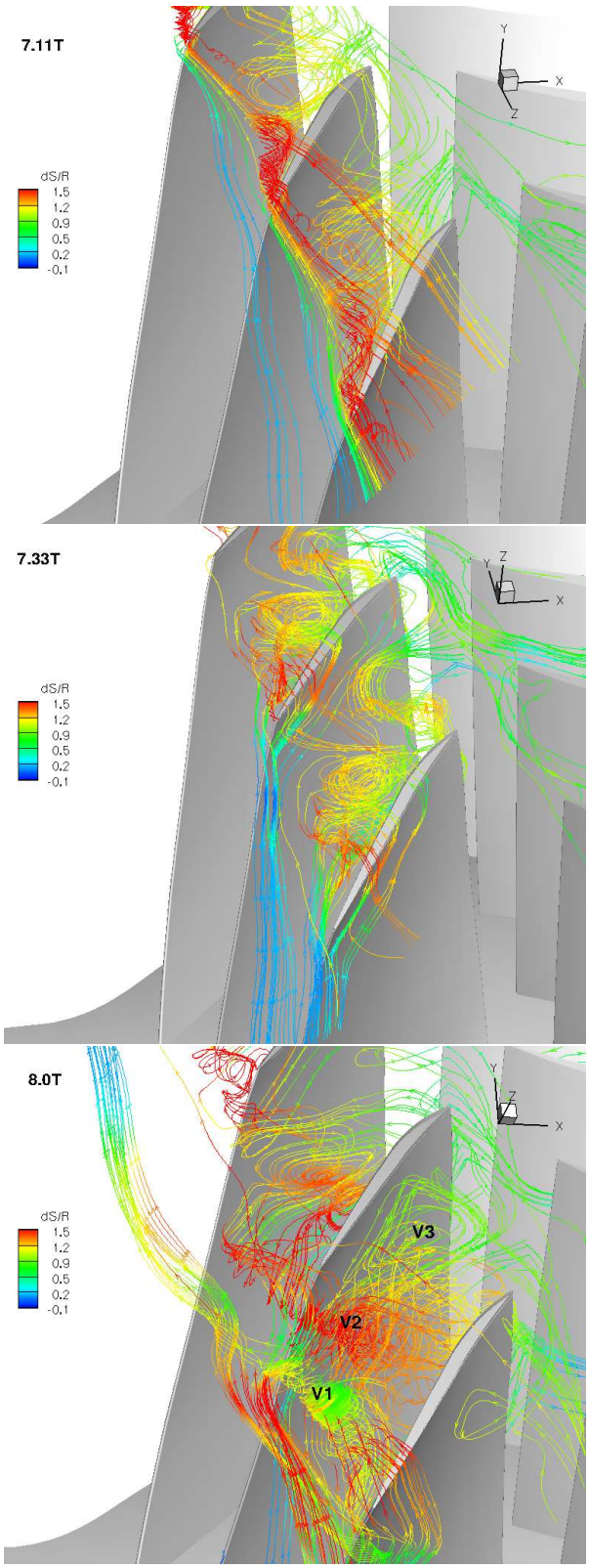

FIGURE 14: Flow structure colored with entropy near tip span